

Dynamical simulations of magnetically channelled line-driven stellar winds – II. The effects of field-aligned rotation

Asif ud-Doula,^{1,2★†} Stanley P. Owocki¹ and Richard H. D. Townsend¹

¹*Bartol Research Institute, University of Delaware, Newark, DE 19716, USA*

²*Department of Physics and Astronomy, Swarthmore College, Swarthmore, PA 19081, USA*

Accepted 2007 December 9. Received 2007 November 30; in original form 2007 September 11

ABSTRACT

Building upon our previous magnetohydrodynamics (MHD) simulation study of magnetic channelling in radiatively driven stellar winds, we examine here the additional dynamical effects of stellar *rotation* in the (still) 2D axisymmetric case of an aligned dipole surface field. In addition to the magnetic confinement parameter η_* introduced in Paper I, we characterize the stellar rotation in terms of a parameter $W \equiv V_{\text{rot}}/V_{\text{orb}}$ (the ratio of the equatorial surface rotation speed to orbital speed), examining specifically models with moderately strong rotation $W = 0.25$ and 0.5 , and comparing these to analogous non-rotating cases. Defining the associated Alfvén radius $R_A \approx \eta_*^{1/4} R_*$ and Kepler corotation radius $R_K \approx W^{-2/3} R_*$, we find rotation effects are weak for models with $R_A < R_K$, but can be substantial and even dominant for models with $R_A \gtrsim R_K$. In particular, by extending our simulations to magnetic confinement parameters (up to $\eta_* = 1000$) that are well above those ($\eta_* = 10$) considered in Paper I, we are able to study cases with $R_A \gg R_K$; we find that these do indeed show clear formation of the *rigid body* disc predicted in previous analytic models, with however a rather complex, dynamic behaviour characterized by both episodes of downward infall and outward breakout that limit the build-up of disc mass. Overall, the results provide an intriguing glimpse into the complex interplay between rotation and magnetic confinement, and form the basis for a full MHD description of the rigid body discs expected in strongly magnetic Bp stars like σ Ori E.

Key words: MHD – stars: early-type – stars: magnetic fields – stars: mass-loss – stars: rotation – stars: winds, outflows.

1 INTRODUCTION

In Paper I of this series (ud-Doula & Owocki 2002), we examined the effect of a large-scale dipole magnetic field on the radiatively driven wind from a hot, massive star. The radiative envelopes of such hot stars means they lack the strong convection zone that drives the dynamo generation of magnetic activity cycles in the Sun and other relatively cool stars. None the less, in recent years spectropolarimetric observations have led to positive detections of large-scale fields in several such hot stars, often well fit by a dipole tilted relative to the star’s rotation axis (e.g. Donati et al. 2002). In some cases the associated period of rotational modulation is quite long, weeks or even years (e.g. in θ^1 Ori C, HD191612; Donati et al. 2006), implying that the direct *dynamical* effect of rotation on the magnetic channelling of the wind is likely to be limited. As a first approximation, the magnetohydrodynamics (MHD) simulation models of Paper I thus ignored the effects of rotation.

More generally, however, massive stars tend to have quite rapid rotation, as evidenced both by the substantial broadening in photospheric spectral lines (Conti & Ebbets 1977; Fukuda 1982), which indicate projected rotation speeds of hundreds of km s^{-1} , and by the relatively short period of observed modulations for some stars, e.g. the magnetic Bp star σ Ori E, for which the inferred rotation period is about 1.2 d (Walborn 1981). Both lines of evidence suggest that hot-star rotation rates are commonly a substantial fraction of the ‘critical’ rate at which the equatorial surface would be in Keplerian orbit. Since this implies centrifugal forces that are comparable to the inward pull of gravity, it is clear that such levels of rotation could significantly influence the magnetic channelling of a stellar wind.

Previous studies have focused in particular on the potential role of magnetic fields in spinning up the wind outflow and channelling it into an equatorial disc that might be centrifugally supported against gravity. Cassinelli et al. (2002) argued that such magnetic spin-up could effectively eject material into a ‘magnetically torqued disc’ (MTD), in which individual fluid elements would be in local Keplerian orbit, and specifically proposed this as a model for the Keplerian ‘decretion discs’ inferred for Be stars. For the

★E-mail: uddoula@morrisville.edu

†Present address: Morrisville State College, Morrisville, NY 13408, USA

chemically peculiar Bp stars that have been directly observed to have very strong magnetic fields ($\gtrsim 10^4$ G), Townsend & Owocki (2005, hereafter TO-05) developed a somewhat different ‘rigidly rotating magnetosphere’ (RRM) paradigm in which the field again spins up and channels wind material into a disc, but now is also sufficiently strong to hold it in *rigid body* rotation. This RRM model has proven particularly successful in explaining the rotationally modulated Balmer emission observed from σ Ori E (Townsend, Owocki & Groote 2005).

To test these semi-analytic paradigms, we have made some initial efforts to extend the numerical MHD simulations of Paper I to include rotation in the simple 2D axisymmetric case of a rotation-aligned dipole. The results indicate that a large-scale field strong enough to torque wind material to Keplerian orbital speed tends also to propel material away from the star, rather than into the kind of stationary, Keplerian disc envisioned in the MTD model (Owocki, Townsend & ud-Doula 2006, 2007; ud-Doula, Townsend & Owocki 2006). However, for cases with strong enough magnetic confinement to hold material down against such outward escape, there can indeed form a limited rigid body disc quite similar to that predicted by the RRM model (Owocki & ud-Doula 2003; Owocki 2006). But even in such cases, there is irregular breakout of material from the outer disc, leading to a sudden magnetic reconnection heating that could explain the hard X-ray flares seen from σ Ori E (ud-Doula et al. 2006).

The present paper further extends these previous MHD simulations with a more extensive 2D parameter study covering models over a range in both rotation rate and degree of magnetic confinement. A particular focus is to develop a clearer physical picture of the complex competition between wind-fed build-up of material in a disc versus losses by both outward ejection and infall back to the star.¹ Moreover, the broad parameter study here allows us to examine in detail how these processes are affected by various combinations of rotation rate and magnetic field strength. To lay the basis for the results presented in Section 4, Section 2 first reviews the general numerical MHD approach and Section 3 defines the overall parameter domain. Section 5 concludes with a summary and outline for future work.

2 NUMERICAL METHOD

2.1 Vector form of basic MHD equations

As in Paper I, our general approach is to use the ZEUS-3D (Stone & Norman 1992) numerical MHD code to evolve a consistent dynamical solution for a line-driven stellar wind from a star with a dipole surface field. Our implementation here again adopts spherical polar coordinates with radius r , colatitude θ and azimuth ϕ , but now in a ‘2.5D’ formulation that allows for non-zero azimuthal components of both the magnetic field B_ϕ and velocity v_ϕ , while still assuming all quantities are constant in the azimuthal coordinate angle ϕ . To maintain this 2.5D axisymmetry, we assume the stellar magnetic field to be a pure dipole with polar axis aligned with the rotation axis of the star.

In vector form, the standard formulation of MHD includes equations for mass continuity,

$$\frac{\partial \rho}{\partial t} + \mathbf{v} \cdot \nabla \rho + \rho \nabla \cdot \mathbf{v} = 0 \quad (1)$$

and momentum balance,

$$\frac{\partial \mathbf{v}}{\partial t} + \mathbf{v} \cdot \nabla \mathbf{v} = -\frac{\nabla p}{\rho} + \frac{1}{4\pi\rho}(\nabla \times \mathbf{B}) \times \mathbf{B} - \frac{GM\hat{\mathbf{r}}}{r^2} + \mathbf{g}_{\text{lines}}, \quad (2)$$

where the notation follows common conventions, and is defined in detail in Section 2 of Paper I. [Note that equation (2) here corrects some minor errors in the corresponding equation (2) of Paper I.]

2.2 Rotation terms in the advective acceleration

The inclusion of a finite rotation in the present work leads to additional nonzero terms proportional to the azimuthal velocity v_ϕ within the three vector components of the advective acceleration,

$$[\mathbf{v} \cdot \nabla \mathbf{v}]_r = v_r \frac{\partial v_r}{\partial r} + \frac{v_\theta}{r} \frac{\partial v_r}{\partial \theta} - \frac{v_\theta^2 + v_\phi^2}{r}, \quad (3)$$

$$[\mathbf{v} \cdot \nabla \mathbf{v}]_\theta = v_r \frac{\partial v_\theta}{\partial r} + \frac{v_\theta}{r} \frac{\partial v_\theta}{\partial \theta} - \cot \theta \frac{v_\phi^2}{r} + \frac{v_r v_\theta}{r}, \quad (4)$$

$$[\mathbf{v} \cdot \nabla \mathbf{v}]_\phi = v_r \frac{\partial v_\phi}{\partial r} + \frac{v_\theta}{r} \frac{\partial v_\phi}{\partial \theta} + \cot \theta \frac{v_\theta v_\phi}{r} + \frac{v_\phi v_r}{r}. \quad (5)$$

The terms here without derivatives represent the inertial forces arising from the curvature of the coordinate system, namely centrifugal and coriolis forces, which, e.g. in the absence of external torques, enforce conservation of angular momentum within the rotating flow described in spherical coordinates.

Of course, in magnetic models the Lorentz force, represented by the second term on the right-hand side of equation (2), can significantly channel the flow, competing against these inertial terms. In rotating models, this Lorentz force can now also impart a significant torque to *spin up* the outflow; moreover it now includes additional terms proportional to the non-zero B_ϕ , which themselves represent a component for outward angular momentum transport.

This competition between the magnetic Lorentz force and the inertia terms associated with *rotation* represents a central focus of the present study. In some ways, it parallels the central competition examined in Paper I, namely between magnetic forces and the inertia associated with the *radial* outflow of the wind.

2.3 Radial driving of wind outflow

This radial outflow arises from the strong radial driving of the line force, $\mathbf{g}_{\text{lines}}$. As in Paper I, we model this here in terms of the standard Castor, Abbott & Klein (1975, hereafter CAK) formalism, corrected for the finite cone angle of the star, using a spherical expansion approximation for the local flow gradients (Pauldrach et al. 1985; Friend & Abbott 1986) and ignoring *non-radial* line force components that can arise in a non-spherical outflow. Although such non-radial terms are typically only a few per cent of the radial force, in non-magnetic models of rotating winds, they act without much competition in the lateral force balance, and so can have surprisingly strong effects on the wind channelling and rotation (Owocki, Cranmer & Gayley 1996; Gayley & Owocki 2000). But in magnetic models with an already strong component of non-radial force, such terms are not very significant, and since their full inclusion substantially complicates both the numerical computation and the analysis

¹ To allow focus on these issues of disc build-up, we defer here any discussion of wind angular momentum loss and the resulting stellar spin-down to a future, follow-up paper.

of simulation results, we have elected to defer further consideration of such non-radial line force terms to future studies.

By limiting our study to moderately fast rotation, half or less of the critical rate, we are also able to neglect the effects of stellar oblateness and gravity darkening.

2.4 Isothermal flow approximation

Another simplification retained from Paper I is that the flow is strictly isothermal. This is generally a reasonable approximation in steady-state, spherical wind models, wherein the competition between photoionization heating and radiative cooling keeps the wind close to the stellar effective temperature (Pauldrach 1987; Drew 1989). However, models with significant magnetic channelling can guide the flow towards strong shock compressions that heat the gas to temperatures of millions of kelvin. The associated extensive X-ray emission (Babel & Montmerle 1997a,b) has indeed been a focus of some of our previous simulations aimed at modelling the observed X-ray spectrum from θ^1 Ori C (Gagné et al. 2005). Moreover, our other simulations show that reconnection heating associated with centrifugally driven breakout events might provide a basis for explaining the relatively hard X-ray flare events seen in the magnetic B-star σ Ori E (ud-Doula et al. 2006).

While such detailed treatments of the wind energy balance can thus be quite important for modelling the X-ray emission from specific stars, including this in the general parameter study here would require introducing an additional free parameter, associated with the wind density, and representing the relative importance of radiative cooling in the post-shock region (ud-Doula 2003). This would in effect require a 3D parameter study, representing cooling, magnetic confinement and rotation. To maintain the focus here on just the one additional degree of freedom associated with rotation, built upon the study of isothermal magnetic confinement in Paper I, we again assume a simple isothermal wind with the wind temperature kept equal to the stellar effective temperature, here taken to be 50 000 K.

A further advantage is that, at such a temperature, the gas pressure terms in equation (2) are typically unimportant throughout most of the supersonic outflow. Thus, although these pressure terms are still fully included in the numerical simulations, they can be largely ignored in interpretation of results, allowing for a focus on the dominant competing forces associated with gravity, radiative driving, magnetic field and flow inertia.

2.5 Boundary conditions and numerical considerations

Finally, numerical specifications such as the computational grid and boundary conditions are again similar to Paper I, except of course that the lower boundary now has a non-zero azimuthal speed $v_\phi(R_*, \theta) = V_{\text{rot}} \sin \theta$, where V_{rot} is the equatorial surface rotation speed. Also, instead of setting the azimuthal field to zero at the stellar surface, as in Paper I, we now compute a generally non-zero B_ϕ at the lower boundary ghost zone by linear extrapolation from the values in the two innermost zones of the actual computational grid. This assumes vanishing second derivatives of the azimuthal field components.

In all simulations presented here the time-step is based on relatively low Courant number of 0.3, a choice that helps ensuring stability and reduced error in computed shock properties (Falle 2002). Simulations of selected models with an even lower Courant number of 0.1 gave very similar results to the standard runs.

3 TWO-PARAMETER STUDY

3.1 Magnetic confinement parameter η_*

Let us now consider how best to frame our parameter study for the combined effects of rotation and magnetic channelling in a line-driven wind. In the absence of significant rotation or magnetic fields, the line force overcomes the stellar gravity to drive a nearly radial wind outflow characterized by a mass-loss rate \dot{M} and terminal wind speed V_∞ . When a magnetic field is added, the inertia of this radial outflow competes against the Lorentz forces. A key result of Paper I is that the overall net effect of a magnetic field in diverting such a wind outflow can be characterized by a single *magnetic confinement parameter*,

$$\eta_* \equiv \frac{B_{\text{eq}}^2 R_*^2}{\dot{M} V_\infty}, \quad (6)$$

where B_{eq} is the surface field strength at the magnetic equator. This sets the scale of the ratio of magnetic energy to wind kinetic energy,

$$\eta(r) \equiv \frac{B^2/8\pi}{\rho v^2/2} = \eta_* \left[\frac{(r/R_*)^{2-2q}}{(1 - R_*/r)^\beta} \right] = \left(\frac{V_A}{v} \right)^2 = M_A^{-2}. \quad (7)$$

The last two equalities emphasize this energy ratio can also be cast as the square of the ratio of the Alfvén speed, $V_A \equiv B/\sqrt{4\pi\rho}$, to flow speed, v , i.e. as the inverse square of the Alfvénic Mach number, $M_A \equiv v/V_A$.

The square bracket factor in the middle equality shows the overall radial variation; q is the power-law exponent for radial decline of the assumed stellar field, e.g. $q = 3$ for a pure dipole, and β is the velocity-law index, with typically $\beta \approx 1$. For a star with a non-zero field, we have $\eta_* > 0$, and so given the vanishing of the flow speed at the atmospheric wind base, this energy ratio always starts as a large number near the stellar surface, $\eta(r \rightarrow R_*) \rightarrow \infty$. But from there outward it declines quite steeply, asymptotically as r^{-4} for a dipole, crossing unity at the Alfvén radius defined implicitly by $\eta(R_A) \equiv 1$.

For a canonical $\beta = 1$ wind velocity law, explicit solution for R_A along the magnetic equator requires finding the appropriate root of

$$\left(\frac{R_A}{R_*} \right)^{2q-2} - \left(\frac{R_A}{R_*} \right)^{2q-3} = \eta_*, \quad (8)$$

which for integer $2q$ is just a simple polynomial, specifically a quadratic, cubic or quartic for $q = 2, 2.5$ or 3 . Even for non-integer values of $2q$, the relevant solutions can be approximated (via numerical fitting) to within a few per cent by the simple general expression,

$$\frac{R_A}{R_*} \approx 1 + (\eta_* + 1/4)^{1/(2q-2)} - (1/4)^{1/(2q-2)}. \quad (9)$$

For weak confinement, $\eta_* \ll 1$, we find $R_A \rightarrow R_*$, while for strong confinement, $\eta_* \gg 1$, we obtain $R_A \rightarrow \eta_*^{1/(2q-2)} R_*$. In particular, for the standard dipole case with $q = 3$, we expect the strong-confinement scaling $R_A/R_* \approx 0.3 + \eta_*^{1/4}$.

Clearly R_A represents the radius at which the wind speed v exceeds the local Alfvén speed V_A . But Paper I showed that it also characterizes the maximum radius where the magnetic field still dominates over the wind, and is just somewhat above (i.e. by 20–30 per cent) the maximum extent of closed loops in the magnetosphere. Moreover, as we shall see below, in rotating winds these closed loop regions tend to corotate nearly rigidly with the underlying star, and in this sense R_A is just above the maximum radius for wind corotation near the equator. For convenience in discussing results, let us thus denote the maximum radius of such closed (and

generally corotating) loops as

$$R_c \approx R_* + 0.7(R_A - R_*) \quad (10)$$

3.2 Rotation parameter W

Let us next seek a similarly convenient parameterization for the stellar rotation. This can again be characterized in terms of a speed, namely the equatorial surface rotation speed V_{rot} . But instead of relating that to the flow speed or Alfvén speed in the stellar *wind*, the stellar origin of rotation suggests it may be better to compare it to a speed representative of the gravity at the stellar *surface*. Specifically, let us thus define our dimensionless rotation parameter as

$$W \equiv \frac{V_{\text{rot}}}{V_{\text{orb}}}, \quad (11)$$

where $V_{\text{orb}} \equiv \sqrt{GM/R_*}$ is the *orbital* speed near the equatorial surface.² This characterizes the azimuthal speed needed for the outward centrifugal forces to balance the stellar surface gravity. It is only a factor of $1/\sqrt{2}$ less than the speed V_{esc} needed to fully *escape* the star's surface gravitational potential.

For a non-magnetic rotating star, conservation of angular momentum in a wind outflow causes the azimuthal speed near the equator to decline outward as $v_\phi \sim 1/r$, meaning that rotation effects tend to be of diminishing importance in the outer wind.

By contrast, in a rotating star with a sufficiently strong magnetic field, magnetic torques on the wind can spin it up; for some region near the star, i.e. up to about the maximum loop closure radius R_c , they can even maintain a nearly rigid body rotation, for which the azimuthal speed now *increases* outward in proportion to the radius,

$$v_\phi(r) = V_{\text{rot}} \frac{r}{R_*}; \quad r \lesssim R_c. \quad (12)$$

As such, even for a star with surface rotation below the orbital speed, $W < 1$, maintaining rigid rotation will eventually lead to a balance between the outward centrifugal force from rotation and the inward force of gravity,

$$\frac{v_\phi^2(R_K)}{R_K} = \frac{GM}{R_K^2}. \quad (13)$$

Combining this with equations (11) and (12) gives a simple expression for the associated ‘Kepler radius’,

$$R_K = W^{-2/3} R_*. \quad (14)$$

Unsupported material at radii $r < R_K$ will tend to fall back towards the star, but any material maintained in rigid rotation to radii $r > R_K$ will have a centrifugal force that *exceeds* gravity, and so will tend to be propelled further outward. Indeed, any corotating material above an ‘escape radius’, which is only slightly beyond the Kepler radius,

$$R_E = 2^{1/3} R_K, \quad (15)$$

will have sufficient rotational energy to escape altogether the local gravitational potential, unless, of course, temporarily held down by the magnetic field.

² This is closely related to the commonly used rotation parameter $\omega \equiv \Omega/\Omega_{\text{crit}}$, defined by the star's angular rotating frequency Ω relative to the value this would have as the star approaches ‘critical’ rotation, Ω_c . Our choice here more directly relates to the additional local speed needed to propel material into Keplerian orbit, and avoids some subtle assumptions (e.g. rigid body rotation using a Roche potential for gravity) about how the global stellar envelope structure adjusts to approaching the critical rotation limit.

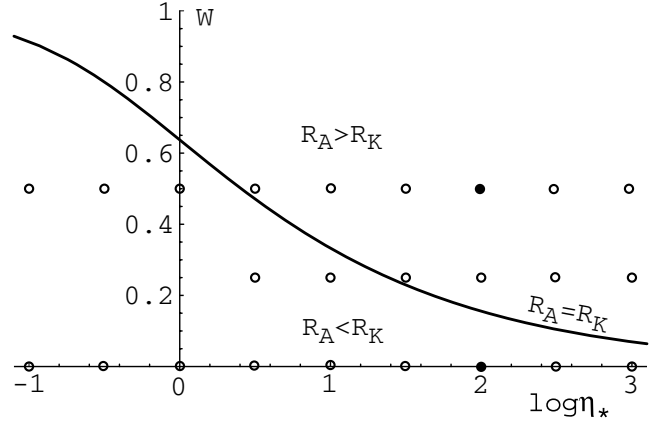


Figure 1. Plot of rotation versus confinement parameter, W versus $\log \eta_*$, to define the models in our 2D parameter study, represented here as filled and open circles, with the filled circles representing models of principal focus for more detailed analyses. The solid curve represents the contour for models with $R_A = R_K$ when the magnetic index is set to the dipole value $q = 3$. Models above this have $R_A > R_K$ and thus strong confinement plus rapid rotation, whereas models below have $R_A < R_K$ and thus either weak-confinement or relatively slow rotation.

3.3 2D parameter grid of models

The circles in Fig. 1 lay out the 2D grid of models computed for the present study, plotted in the plane of rotation parameter W versus \log of the magnetic confinement parameter η_* . The models along the x -axis include several specific cases already examined in the non-rotating study in Paper I, with now however some additional extensions towards the strong-confinement limit, namely $\log \eta_* = 1.5, 2, 2.5$ and 3 . In addition, there are now two new sets of corresponding models with rotation parameters $W = 0.25$ and 0.5 . As noted, we do not consider faster rotation than $W = 0.5$ because this would introduce a significant stellar oblateness that would complicate specification of the lower boundary condition for the spherical coordinate system used in the ZEUS MHD code.

The solid curve in Fig. 1 represents the parameter combination for which $R_A = R_K$ in the dipole case ($q = 3$) with velocity index $\beta = 1$. This contour thus roughly divides the parameter space diagonally: models below and to the left-hand side have only slow rotation and/or weak confinement, and so $R_A < R_K$; models above and to the right-hand side have fast rotation and/or strong confinement, and so $R_A > R_K$.

Our analysis of the associated simulations show that the lower left-hand models give generally quite similar overall structure to what was found for the non-rotating models in Paper I. The more interesting cases are those in the regions above and/or to the right-hand side, and in the transition region with $R_A \approx R_K$.

The transition region represents cases for which the magnetic spin-up is just adequate to propel material into Keplerian orbit. As such, it might seem to be appropriately fine-tuned to produce the kind of MTD advocated by Cassinelli et al. (2002). However, as discussed below and in previous papers (Owocki 2006; Owocki et al. 2006, 2007; ud-Doula et al. 2006), our simulations indicate that even for these optimal parameter cases, the rotating magnetosphere is characterized by a combination of infall and outflow, respectively, below and above the Kepler radius, with no apparent tendency to form an extended, stable, *Keplerian* disc.

On the other hand, in the limit of strong confinement with $R_A \gg R_K$, the dominance of the field can confine the material in a *rigid body*

disc, as postulated in the ‘RRM’ formalism developed by TO-05. The full MHD simulations here allow us to directly test this RRM concept, and define its limitations as wind material accumulates in the disc, leading eventually to a centrifugally driven breakout overcoming the confining magnetic tension (see ud-Doula et al. 2006, and appendix of TO-05). Towards this goal, the magnetic confinement parameters considered here extend to values ($\eta_* = 1000$) that significantly exceed the maximum ($\eta_* = 10$) attempted in the non-rotating study of Paper I.

Such models with strong magnetic confinement are, in fact, significantly more computationally challenging, since the greater rigidity of the magnetic field implies a higher Alfvén speed (see Appendix A), and thus requires a smaller numerical time-step to maintain stability under the Courant criterion. Indeed, this problem is often exacerbated by the tendency for the strong, nearly horizontal field near the magnetic equator to completely inhibit any wind base outflow there; this leads then to short-lived nearly evacuated regions where the Alfvén speed can become exceedingly large, formally even approaching the speed of light! To keep the time-step from becoming too small, we thus choose to artificially add mass to these small evacuated regions at a level that is sufficient to limit the local Alfvén speed to

$$V_A \leq \max(20\,000 \text{ km s}^{-1}, \max(V_{\text{Ap}})), \quad (16)$$

where

$$\max(V_{\text{Ap}}) = 0.65 \sqrt{\eta_*} V_\infty \quad (17)$$

is the expected maximum polar Alfvén speed, as given by the analysis in Appendix A. We check that the amount of artificially added mass is still quite insignificant compared to the global mass-loss in the wind, i.e. less than a per cent in even the most extreme ($\eta_* = 10^3$) cases.

Moreover, the larger Alfvén radius means such models need generally a larger outer boundary radius, and the larger breakout time-scale (as predicted in the appendix of TO-05) means that models have to be run longer to cover the breakout cycles and associated accumulation of mass in any RRM disc. Finally, as discussed further below, the closed magnetic topology of episodic outbursts can complicate the proper specification of the outer boundary condition, and in practice reflection effects as these outbursts are advected through the boundary can occasionally even halt the computation altogether. In summary, the extension of MHD simulations into the very strong-confinement domain remains an ongoing challenge.

3.4 Stellar and wind parameters

Much of the procedures in the current study follows Paper I. Specifically, we use the same standard non-magnetic and *non-rotating* wind model used in Paper I, but now at the initial time we suddenly introduce both a dipole magnetic field, and a *surface rotation* at the lower boundary, with both defined relative to a common polar axis. This standard model has stellar parameters representative of a typical OB supergiant, with a radius $R_* = 19 R_\odot$, a luminosity $L = 10^6 L_\odot$ and an effective mass of $M = 25 M_\odot$. (This reflects a factor of 2 reduction below the Newtonian mass to account for the outward force from the electron scattering continuum.) This radius and mass imply an effective equatorial surface orbital speed of $V_{\text{orb}} \approx 500 \text{ km s}^{-1}$.

The line driving assumes a CAK power index $\alpha = 0.6$ and a line normalization such that the non-magnetic, non-rotating wind has a mass-loss rate of about $\dot{M} \approx 3 \times 10^{-6} M_\odot \text{ yr}^{-1}$ and a terminal speed of about $V_\infty \approx 2400 \text{ km s}^{-1}$. Since both the stellar and wind

parameters are fixed, we vary the magnetic confinement parameter η_* solely through the variations in the assumed equatorial surface field strength, B_{eq} . As noted above, we do not consider rotation parameters $W > 1/2$ since this would deform the stellar surface and require consideration of gravity darkening, neither of which are taken into account in our models.

One further difference compared to the simulations in Paper I is that we find it necessary to run the rotating models here for a longer time in order to identify properties of a relaxed, quasi-stationary asymptotic state (especially for the strong-confinement models). To facilitate comparison among different cases, we standardize a run to duration of $t = 0\text{--}3 \text{ Ms}$, which is already six times longer than the 0.5 Ms used in Paper I. But we have also run selected models for a longer time, e.g. 6 Ms for our standard case with $W = 1/2$ and $\eta_* = 100$. Required run times per model are typically about one to two weeks on a standard workstation.

4 RESULTS

4.1 Corotation and rigid disc

As a standard example to frame the overall study here, let us first focus on this case with confinement $\eta_* = 100$ and rotation $W = 1/2$ ($V_{\text{rot}} = 250 \text{ km s}^{-1}$). Fig. 2 shows a series of time snapshots of the 2D spatial configuration of the magnetic field (solid lines), with the colour scale representing logarithm of density; Fig. 3 gives a similar time sequence for the azimuthal flow speed, scaled relative to the value that would occur in rigid rotation, i.e. $\chi \equiv v_\phi(r)/\Omega r \sin \theta$, where $\Omega \equiv V_{\text{rot}}/R_*$ is the star’s angular rotation frequency. The time snapshots were chosen to illustrate both relatively quiescent intervals (top panels), and phases with dynamic centrifugal breakout (bottom panels). The dashed circle represents the Kepler corotation radius at the equator ($R_K \approx 1.6 R_*$).

In the evolution immediately following the initial condition, the magnetic field channels wind material towards the tops of closed loops near the equator, where the collision with the opposite stream leads to a dense disc-like structure (see top panels). But the gas is also generally torqued by the field, with, as can be seen in the upper panels of Fig. 3, material in the closed magnetosphere up to $R_c \approx 2.7 R_*$ kept nearly in rigid body corotation with the star. Note that these closed, rigidly rotating loops thus extend through and beyond the Kepler radius. For any material trapped on loops below R_K , the outward centrifugal support is less than the inward pull of gravity; since much of this material is compressed into clumps that are too dense to be significantly line driven, it thus eventually falls back to the star following complex patterns along the closed field loops.

By contrast, the dense material *above* the dashed line at R_K has a net radially *outward* force from the centrifugal acceleration versus gravity. Still, during the initial build-up of this material at the tops of loops above R_K , the magnetic field provides tension that is strong enough to hold it down, forming then a segment of the *rigidly rotating disc* predicted in the analytic RRM analysis by TO-05. However, much as anticipated in the appendix of their paper, eventually material in the outer region of this RRM accumulates to sufficient density to force open the magnetic field, leading to the kind of centrifugally driven breakout events simulated in (ud-Doula et al. 2006). This is illustrated here in the bottom panels of Fig. 2.

Note, however, from Fig. 3 that certain regions, marked in blue, actually have a net azimuthal motion that is *against* the sense of the stellar rotation. This surprising and counterintuitive result is not a numerical artefact, but rather is related to a reverse torque effect that occurs in regions of rapid wind acceleration. This was first discussed

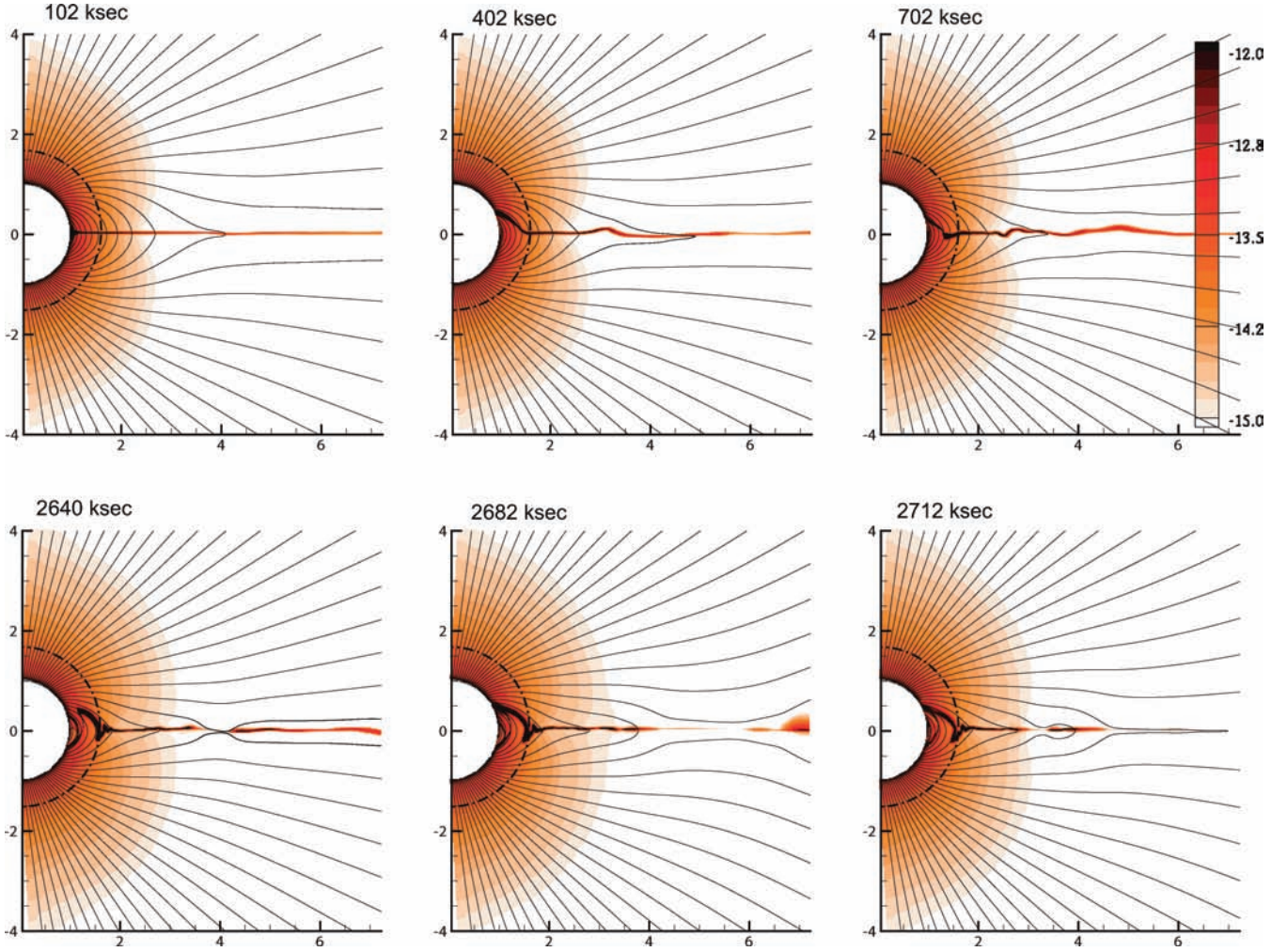


Figure 2. Snapshots of density (in CGS units on a logarithmic colour scale) and field lines (solid lines) at the labelled time intervals for the model with $\eta_s = 100$ and $W = 1/2$. The top panels show the model during a relatively quiescent period, when a dense rigidly rotating disc is being gradually built up. Note, however, that material below the Kepler corotation radius (R_K , shown as a dashed circle) falls back on to the stellar surface, due to the lack of sufficient centrifugal support. The extent of the disc in this phase is determined by the magnetic field strength and extends up to the Alfvén radius $R_A \approx 3.4 R_s$, which is somewhat above the maximum outer radius of closed magnetic loops, R_c . The bottom panels show the model later in the evolution, during one of the episodic centrifugal breakout events.

by MacGregor & Friend (1987), who extended the classic Weber & Davis (1967) 1D magnetic monopole rotation model for the solar wind to the case of the more rapidly accelerating line-driven winds. The 2D analogue for the dipole field here has little impact on our study of rotation and magnetic confinement, and so we defer further discussion to an upcoming paper that focuses on the role of the magnetic field in outward angular momentum transport and stellar spin-down.

The centrifugal breakouts occurring in these simulations necessarily imply a breakdown in the basic formulation for ideal MHD within the ZEUS code. In equatorial regions where the wind or centrifugal terms stretches out field lines of opposite polarity, the finite grid resolution allows effective reconnection, with the associated release of magnetic energy effectively lost instantaneously (e.g. due to radiative cooling) in these isothermal simulations. This is admittedly a simplified representation of the very complex physics thought to occur in actual reconnection, which indeed is an intense area of modern plasma physics research (Shay et al. 1999). But in the present context of *driven* reconnection, the overall global evolution seems

likely to be set by the central competition between magnetic confinement and centrifugal breakout, with relatively little sensitivity to the details of local reconnection sites.

4.2 Global evolution of equatorial disc in radius and time

A key result of the simulations here is that there is really *no true steady state* possible, since the secular build-up of material in the disc must eventually lead to an episodic material breakout once the centrifugal forces overwhelm the finite magnetic tension. One primary goal of the more extensive parameter study here is to examine in detail the nature of this build-up and dissipation of mass in an RRM disc, and how this varies with the changes in the rotation rate and magnetic confinement. To facilitate illustration of these competing processes, let us define a radial mass distribution of the disc, computed at each radius r in terms of the mass within some specified colatitude range about the equator,

$$\frac{dm_e(r, t)}{dr} \equiv 2\pi r^2 \int_{\pi/2 - \Delta\theta/2}^{\pi/2 + \Delta\theta/2} \rho(r, \theta, t) \sin \theta d\theta. \quad (18)$$

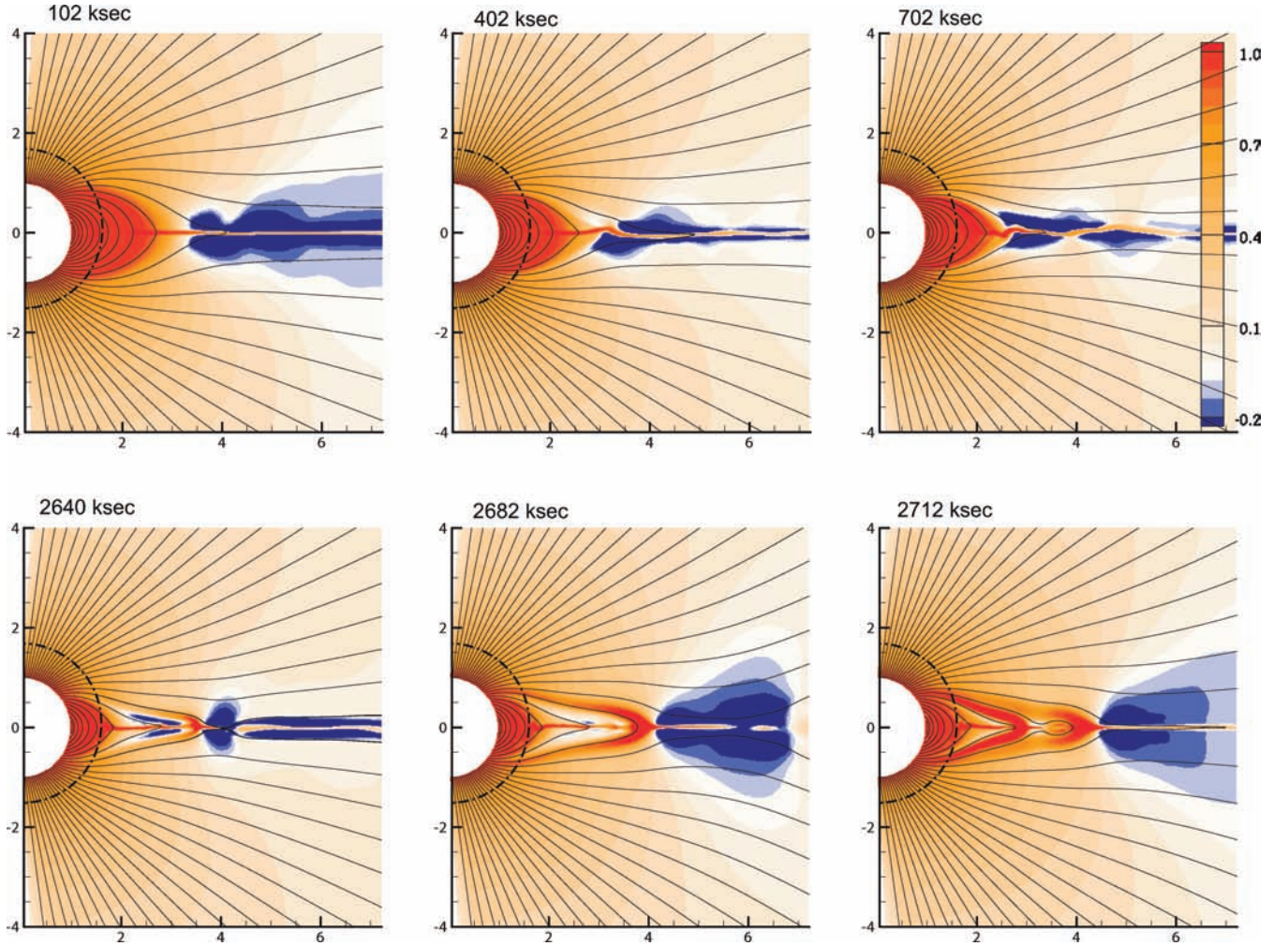


Figure 3. For the same model and same time snapshots as in Fig. 2, the azimuthal speed scaled by the local corotation speed, $\chi \equiv v_\phi / \Omega r \sin \theta$. During the quiescent period the magnetosphere extends nearly to the closure radius $R_c \approx 2.7R_*$, and corotates almost rigidly with the star (top panels). However, during episodic centrifugal breakouts (bottom panels) this RRM shrinks nearly to $R_K \approx 1.6R_*$, represented by the dashed circle. In addition to the mass lost to the breakout, this also helps some of the disc mass to leak inward as infall back on to the star.

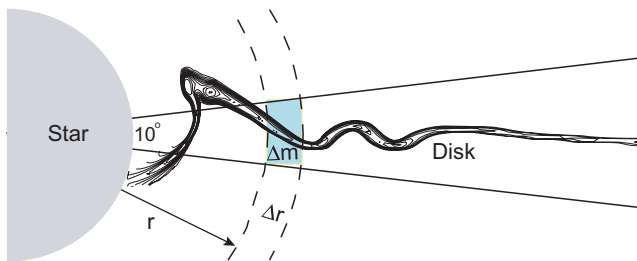


Figure 4. Schematic diagram illustrating the computation of the radial mass distribution of the equatorial disc, dm_e/dr (see equation 18). We choose a cone angle of $\Delta\theta = 10^\circ$ centred on the magnetic equator to encompass most of the material in the disc. We then compute the total mass Δm contained in a narrow strip Δr within the cone. Note, however, that some of the material may not lie within the cone during infalling episodes.

To isolate the disc but not miss too much disc material during various oscillations about the equator, we choose a narrow, but not-too-limited range $\Delta\theta = 10^\circ$. Fig. 4 shows schematically how this is computed.

For the same standard case ($W = 0.5, \eta_* = 100$) shown in Figs 2 and 3, Fig. 5 shows a colour scale plot of this disc mass versus radius (on the ordinate) and time (on the abscissa). The horizontal lines mark, from top to bottom, the estimated Alfvén radius $R_A \approx 3.4R_*$, the loop closure radius R_c , Kepler radius $R_K \approx 1.6R_*$, and inner disc radius, $R_{in} \equiv (2/3)^{1/3} R_K \approx 1.4R_*$ (see equation 19 of TO-05). Within the RRM model, the last represents the location where the effective potential along a rigid field loop first develops a local minimum, which can then trap material fed from the wind.

The plot shows quite succinctly, and vividly, the global time evolution of the equatorial disc material. Initially mass builds up in the region around R_K , but then there appear repeated episodes of infall of inner disc material back on to the star, about every 200 ks or so. This leads to a gradual outward progression to the lower edge of the disc material.

But over a somewhat longer time-scale, about every 1 Ms or so, there appears another, somewhat different kind of disruption, one that starts higher up, closer to the closure and Alfvén radii. This is characterized by outward ejection of the upper disc mass, but then also a ‘rebound’ that propagates back down towards the Kepler radius, pushing the trapped disc material inward, and

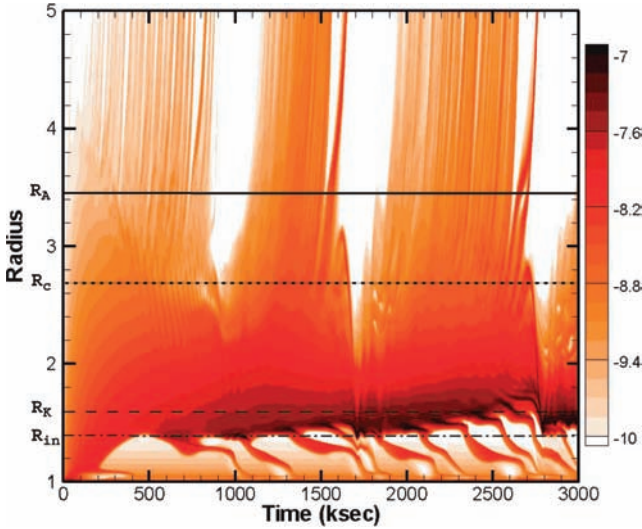


Figure 5. For MHD simulations of the standard model case with $\eta_* = 100$ and $W = 1/2$, the logarithm of the radial distribution of mass, dm_e/dr , within a cone of width $\Delta\theta = 10^\circ$ centred on the equator, plotted versus time and radius (in units of stellar radius). The colour bar shows $\log(dm_e/dr)$ in units of M_\odot/R_* . The horizontal lines indicate the Alfvén radius R_A (solid), the maximum loop closure radius R_c (dotted), the Kepler radius R_K (dashed) and the inner RRM disc radius $R_{in} = (2/3)^{1/3} R_K$ (dot-dashed). Note the accumulation of mass in a disc near the Kepler radius, and how this is limited both by relatively frequent (ca. every 200 ks) intervals of downward infall, and by less frequent (ca. every 1 Ms) major disruptions with substantial upward breakout.

inducing a further leakage of disc mass through downward infall. The overall effect is to regulate the disc mass so that, by the end of the simulation at $t = 3$ Ms, the addition of new material from the wind becomes roughly balanced by the losses to both infall and ejection.

The overall structure is certainly quite dynamic, but near the Kepler radius there none the less appears to be a quasi-permanent disc segment that corresponds roughly to what is predicted by the RRM analytic analysis of TO-05, as well as by the recent time-dependent rigid field hydrodynamics (RFHD) simulations of Townsend, Owocki & ud-Doula (2007).

4.3 Comparison with RRM breakout analysis

Both the RRM and RFHD approaches are based on the idealization that the field is arbitrarily strong, and so remains perfectly rigid regardless of the amount of material in either the wind outflow or the disc build-up. But the associated discussion for both approaches recognized that the secular accumulation of material in the rigid body disc would eventually cause the outward centrifugal forces to overwhelm the available inward tension associated with any large but finite magnetic field. In fact, the appendix of TO-05 presents a simplified, but quantitative analysis of the resulting expected ‘breakout’ of accumulated disc material. This anticipates, at least in general terms, several aspects of the processes seen in the present MHD simulations. In particular, it makes quite specific predictions for both the breakout time-scales as a function of radius, and for the asymptotic mass accumulation near the Kepler radius. In this section, let us thus attempt a specific, semiquantitative comparison between those predictions and the results of the MHD simulations.

4.3.1 Breakout time-scale

Without benefit of the *global* dynamical picture available from the MHD simulations here, the TO-05 breakout analysis focused instead on the conditions for breakout at each *local* radius, conveniently scaled in terms of the Kepler radius as $\xi \equiv r/R_K$. From equation (A6) of TO-05 we find that, in terms of the free-fall time $t_{ff} \equiv R_*/V_{esc}$, the breakout time for some scaled outer disc radius ξ_0 is given by

$$t_b \approx \eta_* t_{ff} \frac{6\xi_*/\xi_0}{\xi_0^3 - 1}. \quad (19)$$

Here we have approximated $\sqrt{\pi}/\mu_* \approx 2$ (cf. equation A8 of TO-05), and used the ratio of wind terminal speed to escape speed, $V_\infty/V_{esc} \approx 3$, to convert the *disc* confinement parameter (also denoted η_*) in TO-05 into the *wind* confinement parameter defined here.³ Note also that the Kepler-scaled stellar radius can be written as $\xi_* = R_*/R_K = W^{2/3}$.

Applying our stellar free-fall time $t_{ff} \approx 19$ ks, then for our standard ($\eta_* = 100$, $W = 1/2$) model, the predicted breakout time is

$$t_b \approx \frac{7 \text{ Ms}}{\xi_0(\xi_0^3 - 1)}. \quad (20)$$

In the MHD simulations for this standard case, the breakouts seem to originate around $R_c \approx 2.7R_*$, for example as indicated in Fig. 5 by the ‘bifurcations’ between upward and downward tracks that start at $r \lesssim 3R_*$ for times around 800, 1600 and 2700 ks. If we thus approximate the outer disc radius by this maximum loop closure radius, we find $\xi_0 = R_c/R_K \approx 1.7$ and so $t_b \approx 1$ Ms, about the time-scale between major breakout eruptions seen in these same MHD simulations.

The TO-05 breakout analysis envisioned a hierarchy of breakout time-scales, with more frequent eruptions occurring at larger radii; but its concluding paragraph also anticipated (partly based on early versions of the MHD simulations described here) that breakouts originating within $r \lesssim 2R_K$ could also lead to substantial disruption of the entire magnetosphere. The simulations here do indeed show such major disruptions, but even after these there remains substantial mass near the Kepler radius.

4.3.2 Accumulated disc mass

For a disc with a scaled outer breakout radius ξ_0 , equation (A10) of TO-05 predicts a specific scaling for the total asymptotic disc mass, which in terms of the parameters here can be written as

$$m_d(\xi_0) = \frac{3\sqrt{\pi} \dot{M} t_{ff} \eta_* W^{4/3}}{\xi_0^2(\xi_0^2 + \xi_0 + 1)} = 2.1 \times 10^{-9} M_\odot \frac{\eta_* W^{4/3}}{\xi_0^2(\xi_0^2 + \xi_0 + 1)}, \quad (21)$$

where the latter gives the numerical scaling for the stellar and wind parameters used here. If we then apply the confinement and parameters of our standard model, and use the characteristic breakout radius $\xi_0 \approx 1.7$ adopted above, we obtain a predicted total disc mass of $m_d \approx 1.6 \times 10^{-8} M_\odot$.

Fig. 6 compares this predicted mass (red horizontal dashed curve) with the time variation of three types of cumulative mass in the standard model MHD results. Specifically, the top curve (black) shows the total integrated mass in the entire grid, including regions

³ Although a footnote in the appendix of TO-05 seems to imply that B_* and B_{eq} are distinct, they are in fact both equal to the field strength at the equatorial surface.

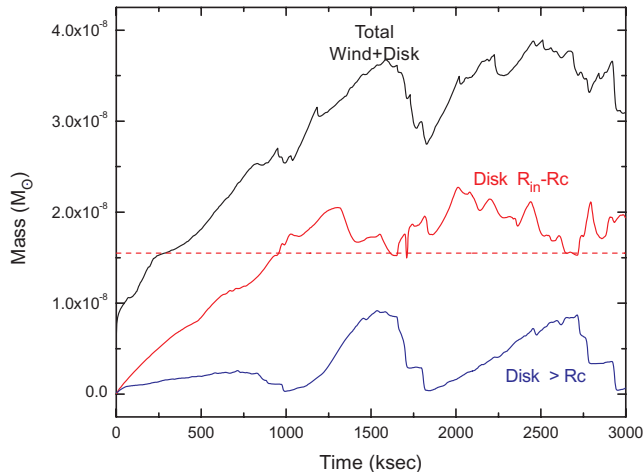


Figure 6. Cumulative mass versus time in MHD simulations for the standard model case. The top curve shows the total mass in the entire grid, i.e. including both disc and wind material. The middle curve shows the disc mass within 5° of the equator, and within radii bounded by the inner RRM disc radius R_{in} and an outer radius $R_o = R_c$. The bottom curve shows equatorial mass above this outer radius. The horizontal dashed line indicates the cumulative disc mass predicted by the RRM breakout analysis, using this same outer radius. Note that it matches quite well the varying asymptotic value of the middle curve, showing the disc mass in the MHD simulation.

of both wind and disc; the middle curve (red) gives the cumulative mass in the equatorial disc region between the inner radius $R_{\text{in}} \approx 0.87R_K \approx 1.4R_*$ and outer radius $R_o \approx R_c \approx 2.7R_*$; and finally, the bottom curve (blue) shows the equatorial mass above this outer disc radius, $r > R_o \approx R_c$.

Note in particular that the predicted asymptotic disc mass agrees remarkably well with this MHD simulation disc mass as shown by the middle, red curve. Of course, this is partly fortuitous, since just a 10 per cent change in the choice of outer disc radius ξ_o would imply a ca. 40 per cent change in disc mass. But the overall, order-magnitude agreement seems likely to be quite robust, and so provides a nice consistency check for both the RRM analysis and numerical simulations.

Comparison of the middle and upper curves in Fig. 6 further shows that the total mass in the thin, radially limited disc represents about half of the total mass in the entire model. In part, this reflects the fact that, for such a strong-confinement model, a large fraction of the outgoing wind gets channelled into the disc. But another factor is that the wind material is flowing outward at a very high speed, and so has a much shorter ‘residency time’ than the trapped, relatively static material in the disc.

4.3.3 Limitations of a localized breakout description

Despite this general success of the local breakout analysis in matching both the overall breakout time-scale and the accumulated disc mass of this MHD simulation, the specifics of the dynamical evolution seen in the simulation make clear that the breakout process is really a *global* phenomenon. As the accumulation of material in the outer disc regions stresses and eventually overcomes the inward restraint of the magnetic field, the associated outward stretching alters the global field, including in the inner regions near the Kepler radius. Moreover, once a breakout occurs, the release of this stretching causes the inner, closed field lines to snap back inward, much like a stretched rubber band after release. The overshoot can push

disc material *below* the Kepler radius and trigger infall back on to the star.

Overall, the wind-fed accumulation of disc mass is thus balanced not just by ejection outward, but also by infall inward. In contrast to the idealized picture of the breakout analysis, which formally predicts the time-scale for breakout (and thus emptying) of material right at the Kepler radius to become arbitrarily long, the dynamic oscillation and associated inward spillage of material limits the asymptotic mass accumulated in this region. This new perspective on the dynamical nature of the disc mass budget has potentially important implications for modelling and interpreting observational diagnostics (see Townsend et al. 2005, 2007).

4.4 Comparison with non-rotating model

To demonstrate further the role of rotation in how magnetic fields influence a wind outflow, let us now compare the results of this $\eta_* = 100$, $W = 1/2$ case with the corresponding non-rotating model. Fig. 7 illustrates the dynamic evolution of equatorial mass for this strong-confinement case without rotation. Comparison with Fig. 5 shows that there are still both breakout and infall episodes, but now with both originating from nearly the same location, at roughly the loop closure radius R_c . This infall from throughout most of the closed field region reflects the lack of any centrifugal support against gravity, and as such, there is no longer any accumulation of material into a circumstellar disc. The breakouts remain, but instead of being driven by centrifugal forces, these are now the result of entrainment of the field with the outflowing wind. The time-scales for both breakout and infall are comparable to the rotating case, but seem somewhat more irregular. Overall, without the build-up in the disc, there is significantly less mass in the magnetosphere than in the rotating case.

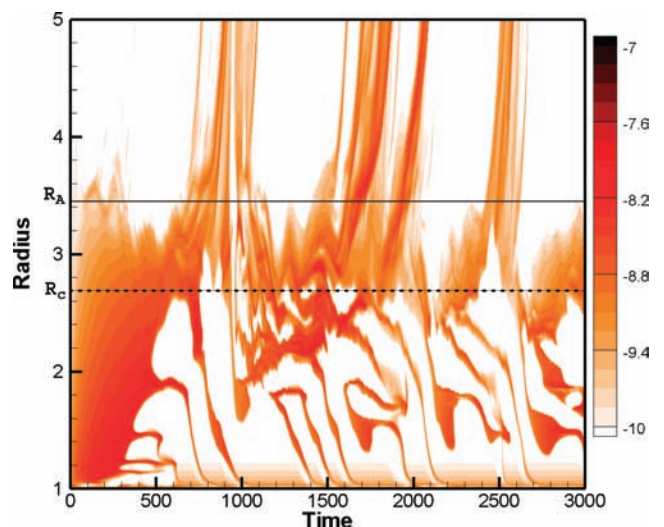


Figure 7. As in Fig. 5, the logarithm of the radial distribution of equatorial mass, $d m_e / d r$, again plotted versus time and radius for a strong confinement ($\eta_* = 100$) model, but now with *no rotation* ($W = 0$). The horizontal lines indicate the Alfvén radius R_A (solid) and loop closure radius R_c (dotted). Note that there are again complex patterns of breakout and infall, but now with more irregular time-scales, and with the infall extending up to regions of breakout, near the loop closure radius. As such, there is no longer an extended region of mass accumulation into a circumstellar disc.

4.5 Results for variation in parameters

To provide a wider context to these detailed results for specific cases with strong confinement, let us now analyse results spanning a broader range of the 2D parameter space for rotation and confinement strength. Before focusing further on equatorial disc material, let us first briefly consider the effects of various magnetic field strengths and rotation rates on the *global* mass-loss from the stellar wind.

4.5.1 Global mass-loss

As discussed in Paper I, one general effect of a strong magnetic field on a wind is the confinement and inhibition of the outflow within a belt around the magnetic equator. For a dipole field line that reaches up to the maximum closure radius R_c , the colatitude θ_c at the surface footpoint satisfies

$$\sin \theta_c = \sqrt{R_*/R_c}. \quad (22)$$

The fraction of the stellar surface area that is covered by closed field lines is given by $\cos \theta_c$, leaving thus only the remaining fraction $1 - \cos \theta_c$ as the source of wind mass-loss. For the non-rotating case, we can thus use this open-field fraction to estimate the overall magnetic reduction in the mass-loss rate,

$$\frac{\dot{M}_B}{\dot{M}_{B=0}} \approx 1 - \sqrt{1 - R_*/R_c}, \quad (23)$$

where R_c is evaluated from equation (10), with the Alfvén radius R_A from equation (9) using $q = 3$. Note that this ignores higher order effects, such as the reduction of the mass flux in open field regions due to the tilt of surface field relative to the radial direction for wind driving (see Owocki & ud-Doula 2004).

The two panels in Fig. 8 compare the mass-loss rate versus $\sqrt{\eta_*} (\propto B)$ for both simple analytic scalings (bottom) and results of numerical MHD simulations (top), with the lower, middle and upper curves in each panel corresponding to the $W = 0, 1/4$ and $1/2$ rotation models. For the non-rotating case, the numerical and analytic results shown in the lower curves are in good overall agreement. But for the rotating case, the upper curves in the top panel show that the tendency of the strong field to reduce the overall mass-loss rate is somewhat compensated by faster rotation, and in the $W = 1/2$ case, even flattens to nearly constant towards the limit of strong confinement. This reflects the additional effect of centrifugal forces in driving the breakout of material initially trapped in closed loops near and below the confinement radius R_c . In effect, the rotation allows eventual breakout from loops that are some factor times the Kepler radius, say $2R_K$.

To take this into account in an analytic scaling formula, the upper two curves in the lower panel use a modified form of equation (23),

$$\frac{\dot{M}_B}{\dot{M}_{B=0}} \approx 1 - \sqrt{1 - R_*/R_c} + 1 - \sqrt{1 - 0.5R_*/R_K}, \quad (24)$$

which effectively sums separate contributions from polar opening and rotational breakout, with the closure and Kepler radii computed from equations (9), (10) and (14). With this generalized scaling, the overall variations of the analytic curves in the lower panel roughly match the corresponding MHD results in the upper panel.

4.5.2 Equatorial mass and disc

Let us next examine how the equatorial disc region is affected by variations in the magnetic confinement and rotation parameters.

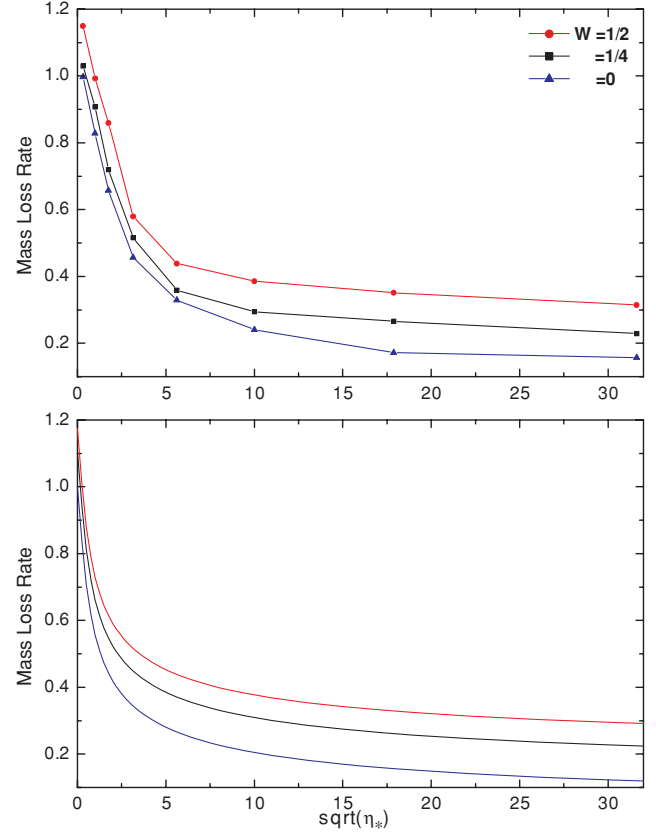


Figure 8. Top panel: Average mass-loss rate (in units of the non-rotating, non-magnetic case) for MHD models with various rotational rates $W = 0, 1/4, 1/2$ plotted against $\sqrt{\eta_*} \propto B_*$. Note that for $W = 1/2$ the mass-loss rate is nearly constant for models with high confinement $\eta_* > 25$. Bottom panel: Corresponding mass-loss rates from the analytic scaling formula in equation (24).

Fig. 9 compares the radius and time evolution of the equatorial mass, dm_e/dr , for an mosaic of models with various η_* and W . The comparison provides a global overview of how the equatorial mass evolution is affected by changes in confinement and rotation.

For weak rotation and confinement cases in the lower left-hand panels, material generally escapes outward without much infall, with only a modest rotational enhancement in mass-loss. But most other models again show a complex competition between infall and breakout, with the latter always being less frequent and stronger.

In particular, this complex combination of infall and breakout also dominates the $R_A \approx R_K$ transition models identified in Fig. 1, i.e. the ones here with $\log \eta_* = 1/2$ and $W = 1/2$ or $\log \eta_* = 3/2$ and $W = 1/4$. Such models might seem optimally fine-tuned to propel material into Keplerian orbit, and yet they show no apparent tendency for material to accumulate into the extended, Keplerian disc envisioned in the MTD scenario suggested by Cassinelli et al. (2002). The lack of a sharp outer cut-off in the large-scale dipole field makes it incompatible with the shear of a Keplerian disc, and without the closed loops that hold down a rigid disc in the strong-confinement limit, material is propelled outward to escape, rather than into a stable Keplerian orbit.

As expected, accumulation into such a rigid body disc is the strongest for the fastest rotation, and the strongest confinement, as shown by models at the upper right-hand side. For strong confinement but slow or no rotation, the material infall comes from a greater

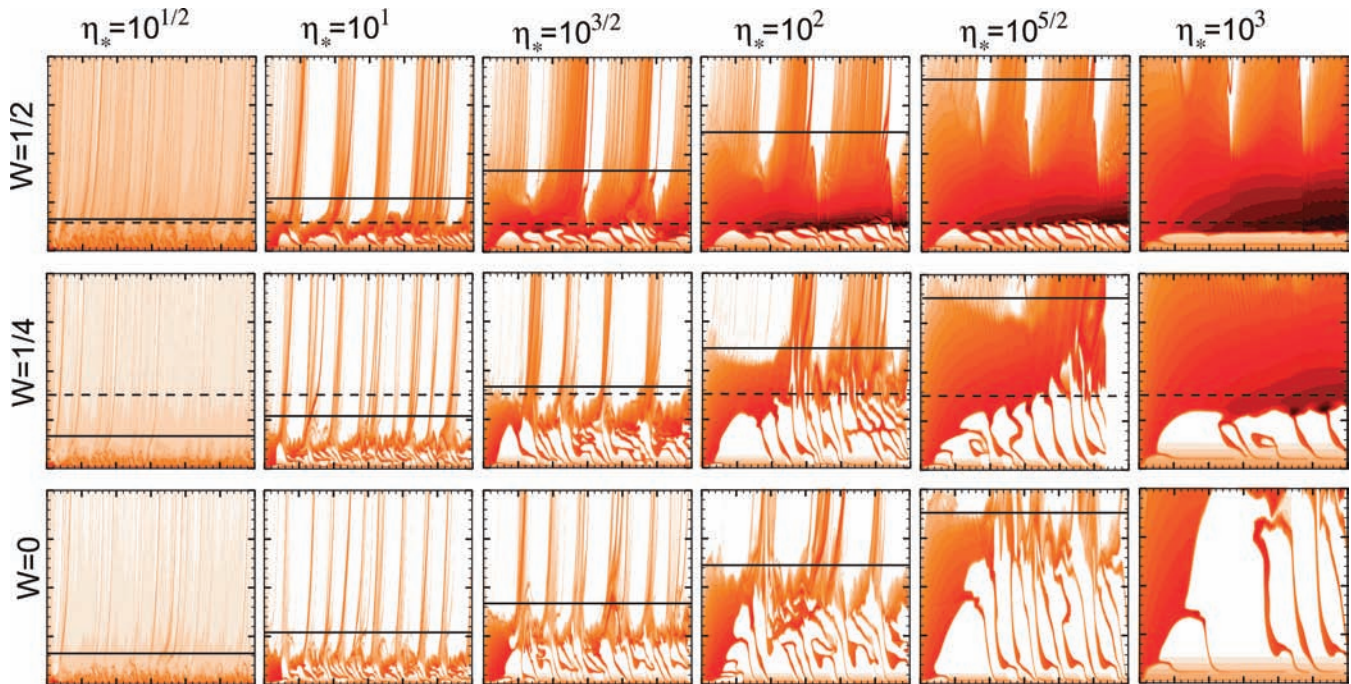


Figure 9. Logarithm of radial distribution of equatorial disc mass, $d m_e / d r$ versus radius and time, for a mosaic of models with magnetic confinements $\log(\eta_*) = 1/2, 1, 3/2, 2, 5/2$ and 3 (columns from left-hand side) and rotations $W = 0, 1/4$ and $1/2$ (rows from bottom) with the same contour levels and the ranges for time and radius as in Fig. 5. Again, the horizontal lines indicate the Alfvén radius R_A (solid) and the Kepler radius R_K (dashed).

height, set by the closure radius, which increases roughly as $R_c \sim \eta_*^{1/4}$.

This larger infalling height seems also to lead to a somewhat longer infalling time-scale. Likewise, the breakout time-scale also seems to increase for models with stronger confinement parameter η_* , but not quite in the linear proportion that might be suggested by equation (19). The reason is that the scaled outer confinement radius ξ_0 appears in the denominator, and since this also increases with confinement through its dependence on the closure radius R_c , the net effect is to weaken the η_* sensitivity of t_b , especially in the strong-confinement limit $\eta_* \gg 1$.

Note also that the $W = 1/2$ rotation model with the strongest confinement, $\eta_* = 1000$, is relatively stable, without the repeated equatorial infalling events seen in other models. Instead of the extensive north–south disc oscillations seen in other models, in this case the variations of the equatorial disc are mostly symmetric about the equator, and thus do not induce as much ‘spillage’ back on to the star. The recent analysis of ‘RFHD’ models by Townsend et al. (2007) show that both types of oscillation modes are allowed, with the one dominating in simulations depending on subtle details of the excitation processes.

But overall, it seems that the basic principals gleaned from the detailed study of the standard, strong-confinement case can be quite logically generalized to understand the trends in properties seen from this mosaic of models spanning a broad range of rotation and confinement parameters.

5 SUMMARY AND FUTURE WORK

This paper examines the effects of field-aligned rotation on the magnetic channelling and confinement of a radiatively driven stellar wind. It builds upon the non-rotating models of Paper I, extending

them to cases of much stronger magnetic confinement (up to $\eta_* = 1000$), and comparing a full spectrum of models ranging from weak to strong confinement at equatorial rotation rates from zero to a substantial fraction ($W = 1/4$ and $1/2$) of the critical (or orbital) limit. As an initial study, it ignores the effects of oblateness, gravity darkening and limb darkening, and is based on an idealization of isothermal flow driven by a purely radial line force.

The key results can be summarized as follows.

- (i) The 2D parameter space represented by rotation W and magnetic confinement η_* can be conveniently divided by comparing the Kepler radius $R_K \approx W^{-2/3} R_*$ with the Alfvén radius $R_A \approx \eta_*^{1/4} R_*$.
- (ii) Models with $R_A < R_K$ have weak rotation and/or magnetic confinement, with the effects of rotation limited to some modest enhancement in equatorial density and overall mass-loss rate, relative to non-rotating cases. In general any magnetically confined material falls back to the star.
- (iii) Transition models with $R_A \approx R_K$ have a complex combination of inner region infall and outer region breakout, but show no signs of accumulation of material into the kind of extended Keplerian disc posited in the MTD paradigm of Cassinelli et al. (2002).
- (iv) In models with $R_A > R_K$ the strong magnetic confinement combines with a sufficiently rapid rotation that can support material against infall near and above the Kepler radius, with then the magnetic field both holding material in nearly rigid body rotation, and keeping it confined against the tendency for the centrifugal force to propel material outward against gravity.
- (v) Such strongly confined rotation models show a clear accumulation into a *rigid body* disc, much as predicted in the analytic RRM formalism of TO-05.
- (vi) However, the present MHD simulations show that such rigid body discs can be highly dynamic and variable, with mass accumulation regulated by a complex combination of inner disc infall and outer disc breakout.

(vii) None the less, application of the simple breakout analysis introduced by TO-05 – slightly modified to identify the outer disc limit with the maximum radius of loop closure – provides a quite good, semiquantitative agreement with both the breakout time-scale and limiting disc mass of the MHD simulations.

(viii) The breakout events here are similar to those discussed by ud-Doula et al. (2006), except the assumption here of isothermal flow precludes us from following that paper's specific application to modelling X-ray flares.

There thus remains much work for future extensions of the present study, including relaxation of the assumptions of isothermal flow, purely radial driving, 2D axisymmetry with aligned dipole field and moderate rotation rates for which stellar oblateness can be neglected.

To more fully test the RRM paradigm, there is also a need to extend MHD simulations even further into the large confinement limit, to approach as closely as possible the estimated $\eta_* \approx 10^7$ appropriate for Bp stars like σ Ori E.

But even within the context the present set of models, we have ignored here another key effect of magnetic rotation, namely the outward angular momentum loss in the stellar wind, and the associated spin-down of the underlying star. This omission was made to allow a more directed focus on the already quite interesting, complex and subtle effects of rotation on magnetic confinement and disc formation. But we have already carried out an extensive analysis of the implications of our study for angular momentum loss and stellar spin-down, and so intend this to be the subject for the next paper in this series.

ACKNOWLEDGMENTS

This work was carried out with partial support by NASA Grants Chandra/TM7-8002X and LTSA/NG05GC36G, and by NSF grant AST-0507581. We thank D. Cohen, M. Gagné, D. Mullan, A. J. van Marle and A. Okazaki for many helpful discussions.

REFERENCES

- Babel J., Montmerle T., 1997a, *ApJ*, 485, L29
 Babel J., Montmerle T., 1997b, *A&A*, 323, 121
 Cassinelli J. P., Brown J. C., Maheswaran M., Miller N. A., Telfer D. C., 2002, *ApJ*, 578, 951
 Castor J. I., Abbott D. C., Klein R. I., 1975, *ApJ*, 195, 157 (CAK)
 Conti P. S., Ebbets D., 1977, *ApJ*, 213, 438
 Donati J.-F., Babel J., Harries T. J., Howarth I. D., Petit P., Semel M., 2002, *MNRAS*, 333, 55
 Donati J.-F. et al., 2006, *MNRAS*, 370, 629
 Drew J. E., 1989, *ApJS*, 71, 267
 Falle S. A. E. G., 2002, *ApJ*, 577, L123
 Friend D. B., Abbott D. C., 1986, *ApJ*, 311, 701
 Fukuda I., 1982, *PASP*, 94, 271
 Gagné M., Oksala M. E., Cohen D. H., Tonnesen S. K., ud-Doula A., Owocki S. P., Townsend R. H. D., MacFarlane J. J., 2005, *ApJ*, 628, 986
 Gayley K. G., Owocki S. P., 2000, *ApJ*, 537, 461
 MacGregor K. B., Friend D. B., 1987, *ApJ*, 312, 659
 Owocki S., 2006, in Kraus M., Miroshnichenko A. S., eds, *ASP Conf. Ser. Vol. 355, Formation and Evolution of Discs around Classical Be Stars*. Astron. Soc. Pac., San Francisco, p. 219
 Owocki S., ud-Doula A., 2003, in Balona L. A., Henrichs H. F., Medupe R., eds, *ASP Conf. Ser. Vol. 305, Magnetic Spin-Up of Line-Driven Stellar Winds*. Astron. Soc. Pac., San Francisco, p. 350
 Owocki S. P., ud-Doula A., 2004, *ApJ*, 600, 1004
 Owocki S. P., Cranmer S. R., Gayley K. G., 1996, *ApJ*, 472, L115

- Owocki S., Townsend R., ud-Doula A., 2006, in 36th COSPAR Sci. Assembly, CD-ROM Meeting Abstract 3548
 Owocki S., Townsend R., ud-Doula A., 2007, *Phys. Plasmas*, 14, 056502
 Pauldrach A., 1987, *A&A*, 183, 295
 Pauldrach A., Puls J., Hummer D. G., Kudritzki R. P., 1985, *A&A*, 148, L1
 Shay M. A., Drake J. F., Rogers B. N., Denton R. E., 1999, *Geophys. Res. Lett.*, 26, 2163
 Stone J. M., Norman M. L., 1992, *ApJS*, 80, 753
 Townsend R. H. D., Owocki S. P., 2005, *MNRAS*, 357, 251 (TO-05)
 Townsend R. H. D., Owocki S. P., Groote D., 2005, *ApJ*, 630, L81
 Townsend R. H. D., Owocki S. P., ud-Doula A., 2007, *MNRAS*, 382, 13
 ud-Doula A., 2003, PhD thesis, Univ. Delaware
 ud-Doula A., Owocki S. P., 2002, *ApJ*, 576, 413
 ud-Doula A., Townsend R. H. D., Owocki S. P., 2006, *ApJ*, 640, L191
 Walborn N. R., 1981, *ApJ*, 243, L37
 Weber E. J., Davis L. J., 1967, *ApJ*, 148, 217

APPENDIX A: MAXIMUM POLAR ALFVÉN SPEED

We derive here equation (17) cited in Section 3.3, giving a simple scaling relation between the expected maximum polar Alfvén speed and the wind magnetic confinement parameter. We begin by repeating equation (7) relating the ratio of magnetic to wind energy density to the ratio of Alfvén speed to flow speed,

$$\eta(r) \equiv \frac{B^2/8\pi}{\rho v^2/2} = \left(\frac{V_A}{v} \right)^2. \quad (\text{A1})$$

Here the density ρ can be eliminated by noting that, for a steady-state, magnetically channelled flow, the lack of divergence in both the field and mass flux requires

$$\frac{4\pi\rho v}{B} = \text{constant} \equiv \frac{\dot{M}}{B_p R_*^2}, \quad (\text{A2})$$

where we have normalized in terms of a polar surface field B_p and global mass flux \dot{M} . For a polar field that declines with radius as $B = B_p (R_*/r)^q$, this gives for the polar Alfvén speed,

$$V_{Ap}^2 = \frac{B_p R_*^2}{\dot{M}} B v = 4\eta_* \left(\frac{R_*}{r} \right)^q v V_\infty, \quad (\text{A3})$$

where the latter equality casts this in term of the magnetic confinement parameter, with the factor of 4 correcting for the fact that our standard η_* is defined in terms of the equatorial surface field B_{eq} , which is half the polar value B_p . If we further assume a standard $\beta = 1$ velocity law, then

$$V_{Ap} = 2\sqrt{\eta_*} V_\infty \left(1 - \frac{R_*}{r} \right)^{1/2} \left(\frac{R_*}{r} \right)^{q/2}. \quad (\text{A4})$$

Setting the radial derivative of this to zero shows that the maximum occurs at radius $r = (1 + 1/q) R_*$, i.e. at $r = (4/3) R_*$ for the standard dipole case with $q = 3$. Plugging this radius into equation (A4), we find that the expected maximum Alfvén speed for dipole expansion of the polar wind is

$$\max(V_{Ap}) = \frac{\sqrt{27}}{8} \sqrt{\eta_*} V_\infty \approx 0.65 \sqrt{\eta_*} V_\infty. \quad (\text{A5})$$

This thus provides a simple rule for the maximum Alfvén speed to allow in running MHD simulations with increasing magnetic confinement parameter, as discussed in Section 3.3.

This paper has been typeset from a \LaTeX file prepared by the author.